

Interpolation of missing electrode data in electrical impedance tomography[‡]

Bastian Harrach¹

¹ Institute of Mathematics, Goethe University Frankfurt, Germany

E-mail: harrach@math.uni-frankfurt.de

Abstract. Novel reconstruction methods for electrical impedance tomography (EIT) often require voltage measurements on current-driven electrodes. Such measurements are notoriously difficult to obtain in practice as they tend to be affected by unknown contact impedances and require problematic simultaneous measurements of voltage and current.

In this work, we develop an interpolation method that predicts the voltages on current-driven electrodes from the more reliable measurements on current-free electrodes for difference EIT settings, where a conductivity change is to be recovered from difference measurements. Our new method requires the a-priori knowledge of an upper bound of the conductivity change, and utilizes this bound to interpolate in a way that is consistent with the special geometry-specific smoothness of difference EIT data.

Our new interpolation method is computationally cheap enough to allow for real-time applications, and simple to implement as it can be formulated with the standard sensitivity matrix. We numerically evaluate the accuracy of the interpolated data and demonstrate the feasibility of using interpolated measurements for a monotonicity-based reconstruction method.

AMS classification scheme numbers: 35R30, 35R05 35J25

1. Introduction

Electrical impedance tomography (EIT) is a novel technique that images the conductivity distribution inside a subject from electric voltage and current measurements on the subject's boundary. EIT has promising applications in several fields including medical imaging, geophysics, nondestructive material testing and monitoring of industrial processes. For a broad overview on the developments in EIT in the last decades let us refer to [35, 5, 75, 64, 61, 12, 8, 9, 59, 36, 7, 73, 1, 60, 69], and the references therein.

The inverse problem of reconstructing the conductivity from voltage-current-measurements is known to be highly ill-posed and non-linear, and the reconstructions suffer from an enormous sensitivity to modeling and measurement errors. To alleviate

[‡] This is an author-created, un-copyedited version of an article published in *Inverse Problems* **31**(11), 115008, 2015. IOP Publishing Ltd is not responsible for any errors or omissions in this version of the manuscript or any version derived from it. The Version of Record is available online at <http://dx.doi.org/10.1088/0266-5611/31/11/115008>.

this problem, most applications concentrate on reconstructing a conductivity change from the difference of two measurements, which is less affected by modeling errors, cf. the above cited works for time-difference EIT and [68, 29, 31] for weighted frequency-difference EIT. In some applications one may further restrict the problem to recovering only the outer support of the conductivity change (the so-called anomaly or inclusion detection problem), which is unaffected by linearization errors, cf. [30].

In practice, the inverse problem of difference EIT is usually linearized, and the conductivity change is then recovered from minimizing a regularized version of the linearized residuum functional, see subsection 2.2. This approach is well-established and very flexible as it can incorporate all available measurements in the residuum functional. However, there is almost no theoretical justification for this approach. Standard convergence results for linearization-based iterative solvers for non-linear inverse problems are based on certain assumptions, the so-called source conditions and the tangential cone condition. It is not clear, whether realistic conductivity distributions fulfill the required abstract source conditions, and the validity of the tangential cone condition is a long-standing open problem in EIT, cf. [58] for a recent contribution.

On the other hand, rigorously justified reconstruction methods for EIT have been developed in the more mathematically-oriented community. An explicit reconstruction formula that is based on the global uniqueness proof of Nachman [62] is known as the \bar{d} -method, cf., e.g., [70, 51, 52, 55, 46, 56, 47, 53, 54]. Rigorously justified inclusion detection methods for EIT include the enclosure method (see [41, 10, 42, 44, 43, 45, 39, 74, 38]), the Factorization Method (see [21, 14, 49, 4, 24, 37, 57, 63, 16, 15, 18, 29, 66, 31, 67, 17, 11, 13, 6] and the recent overviews [50, 23, 27]), and the recently emerging Monotonicity Method [72, 71, 32, 76].

Rigorously justified reconstruction methods rely on interpreting the measurements as (an approximation to) the continuous Neumann-to-Dirichlet (NtD) operator of the underlying partial differential equation, and the operator structure plays a major role in the methods' theoretical foundation. In practical EIT applications, the continuous NtD-operator has to be replaced by the discrete matrix of voltage-current measurements on a finite number of electrodes. Still, in that case certain rigorous properties can be guaranteed, cf. [33], and rigorously justified methods have successfully been applied to real data situations, cf., e.g. [4, 31, 76].

Practical applications of rigorously justified methods require, however, a full matrix of measurements that includes voltages on current-driven electrodes. Such measurements are notoriously difficult to obtain in practice as they tend to be affected by unknown contact impedances and require problematic simultaneous measurements of voltage and current. Accordingly, there is a long-standing disagreement in the engineering community whether practical EIT systems should take voltage measurements on current-driven electrodes. Some groups have successfully developed systems that utilize these measurements, cf. Rensselaer's ACT 4 system [65] or the system of the Dartmouth group [19, 20]. However, in several other systems, including the recently commercially launched PulmoVista[®] 500 from Dräger Medical, voltage measurements

on current-driven electrodes are not taken.

In this work, we develop an interpolation method that predicts the voltages on current-driven electrodes from the more reliable measurements on current-free electrodes for difference EIT settings, where a conductivity change is to be recovered from difference measurements. Our new method is based on utilizing the special geometry-specific smoothness of difference EIT data in the following way. The difference of two electric potentials for different conductivities solves an elliptic PDE with homogeneous boundary data and a source term generated by the conductivity change. The smoothness of the measured boundary voltage differences will depend on how far the conductivity change is supported away from the boundary. We assume the a-priori knowledge of an upper bound B of the conductivity change. With this bound we calculate minimal source terms on B that are consistent with the measurements on the current-free electrodes. The minimal measurement-consistent source terms are then used to calculate the missing voltages on the current-driven electrodes.

We will show that this new interpolation procedure uniquely determines the missing voltages on current-driven electrodes, and derive an analytic formula to calculate the interpolated voltages. Notably, our new interpolation method is computationally cheap enough to allow for real-time applications, and simple to implement as it can be formulated with the standard sensitivity matrix. For a setting with m electrodes, the interpolated voltages can be obtained by solving a linear system with a $m \times m$ -matrix that is constructed from the columns of the sensitivity matrix, see theorem 3.4 and remark 3.5 for the details.

The paper is organized as follows. In section 2, we describe a typical difference EIT setting with adjacent-adjacent current driving patterns, and summarize the standard linearized reconstruction method and the novel matrix-based monotonicity method. Section 3 contains our main result on how to interpolate the voltages on current-driven electrodes using geometry-specific smoothness of difference EIT data. In section 4, we illustrate our new interpolation method and numerically evaluate the interpolation error. We also demonstrate the feasibility of using interpolated measurements for a monotonicity-based reconstruction method for two- and three-dimensional numerical examples.

2. Missing electrode data in electrical impedance tomography

2.1. The setting

Let $\Omega \subset \mathbb{R}^n$, $n \geq 2$ be a bounded domain describing the imaging domain and let $\sigma \in L_+^\infty(\Omega)$ be its conductivity distribution. Ω is assumed to have piecewise smooth boundary $\partial\Omega$ with outer normal vector ν . L_+^∞ denotes the subspace of L^∞ -functions with positive essential infima.

For electrical impedance tomography (EIT), several electrodes $\mathcal{E}_l \subset \partial\Omega$, $l = 1, \dots, m$, are attached to the imaging domain's surface. We assume that the electrodes

E_l are relatively open and connected subsets of $\partial\Omega$, that they are perfectly conducting and that contact impedances are negligible (the so-called *shunt model*, cf., e.g., [12]). When a current $I_l \in \mathbb{R}$ is driven through the l -th electrode, with $\sum_{l=1}^m I_l = 0$, the electric potential inside the imaging domain is given by the solution $u_\sigma \in H^1(\Omega)$ of

$$\nabla \cdot (\sigma \nabla u_\sigma) = 0 \quad \text{in } \Omega, \quad (1)$$

$$\int_{\mathcal{E}_l} \sigma \partial_\nu u_\sigma \, ds = I_l \quad \text{for } l = 1, \dots, m, \quad (2)$$

$$\sigma \partial_\nu u_\sigma = 0 \quad \text{on } \partial\Omega \setminus \bigcup_{l=1}^m \mathcal{E}_l, \quad (3)$$

$$u_\sigma|_{\mathcal{E}_l} = \text{const.} \quad \text{for all } l = 1, \dots, m. \quad (4)$$

u_σ is uniquely determined up to the addition of constant functions.

In a standard adjacent-adjacent driving configuration the voltage-current-measurements are carried out in the following way. For each $k = 1, \dots, m$, we drive a current of $I_k = 1$ and $I_{k+1} = -1$ through the k -th pair of electrodes $(\mathcal{E}_k, \mathcal{E}_{k+1})$ while all other electrodes are kept insulated. Here, and throughout the paper, the electrode index is always considered modulo m , i.e. the index $m+1$ refers to the first electrode, and the index 0 refers to the m -th electrode.

The resulting electric potential $u^{(k)}$ solves (1)–(4) with

$$I_l := \delta_{k,l} - \delta_{k+1,l} \quad \text{for } l = 1, \dots, m.$$

While keeping up the electric current between the k -th electrode pair, we measure the voltage between the j -th pair of electrodes, i.e.,

$$U_{jk}(\sigma) := u_\sigma^{(k)}|_{\mathcal{E}_j} - u_\sigma^{(k)}|_{\mathcal{E}_{j+1}}. \quad (5)$$

Repeating this process for all $j, k = 1, \dots, m$ we obtain the measurement matrix

$$U(\sigma) = \begin{pmatrix} \begin{matrix} U_{11}(\sigma) & U_{12}(\sigma) & U_{13}(\sigma) & \dots & U_{1,m-1}(\sigma) & U_{1,m}(\sigma) \\ U_{21}(\sigma) & U_{22}(\sigma) & U_{23}(\sigma) & \dots & U_{2,m-1}(\sigma) & U_{2,m}(\sigma) \\ U_{31}(\sigma) & U_{32}(\sigma) & U_{33}(\sigma) & \ddots & & U_{3,m}(\sigma) \\ \vdots & \vdots & \ddots & \ddots & \ddots & \vdots \\ U_{m-2,1}(\sigma) & U_{m-2,2}(\sigma) & & \ddots & U_{m-2,m-1}(\sigma) & U_{m-2,m}(\sigma) \\ U_{m-1,1}(\sigma) & U_{m-1,2}(\sigma) & U_{m-1,3}(\sigma) & \dots & U_{m-1,m-1}(\sigma) & U_{m-1,m}(\sigma) \\ U_{m,1}(\sigma) & U_{m,2}(\sigma) & U_{m,3}(\sigma) & \dots & U_{m,m-1}(\sigma) & U_{m,m}(\sigma) \end{matrix} \end{pmatrix}$$

The gray marked entries U_{jk} with $|j - k| \leq 1$ (modulo m) correspond to voltage measurements on current-driven electrodes. In practice, these measurements are usually considered erroneous since they tend to be affected by contact impedances that are not considered in the model and require problematic simultaneous measurement of voltage and current.

Note that the measurement matrix contains some redundancy. Using (1)–(4) one can show that

$$U_{jk}(\sigma) = \int_{\Omega} \sigma \nabla u_\sigma^{(j)} \cdot \nabla u_\sigma^{(k)} \, dx = U_{kj}(\sigma),$$

so that $U(\sigma) \in \mathbb{R}^{m \times m}$ is symmetric. Moreover, it immediately follows from (5) that the entries of each column in $U(\sigma)$ sum to zero. Hence, without voltage measurements on current-driven electrodes, essentially m entries are missing in $U(\sigma)$.

2.2. Linearized reconstruction methods for difference EIT

In difference EIT, one compares two voltage measurements $U(\sigma)$, $U(\sigma_0)$ to reconstruct the conductivity change $\sigma - \sigma_0$ with respect to some reference conductivity distribution σ_0 . In a standard linearized approach, one obtains an approximation κ to the conductivity change by solving (a regularized version of) the linearized equation

$$U'(\sigma_0)\kappa = V \quad (6)$$

where $V := U(\sigma) - U(\sigma_0)$ is the difference of the measured data, and $U'(\sigma_0) : L^\infty(\Omega) \rightarrow \mathbb{R}^{m \times m}$ is the Fréchet derivative of the voltage measurements,

$$U'(\sigma_0) : \kappa \mapsto \left(- \int_{\Omega} \kappa \nabla u_{\sigma_0}^{(j)} \cdot \nabla u_{\sigma_0}^{(k)} \, dx \right)_{j,k=1,\dots,m} \in \mathbb{R}^{m \times m},$$

where $u_{\sigma_0}^{(j)}$ solves (1)–(4) with reference conductivity σ_0 and electric current driven through the j -th and $(j+1)$ -th electrode.

We discretize the imaging domain $\bar{\Omega} = \bigcup_{i=1}^r P_i$ into r disjoint pixels P_i and assume that κ is piecewise constant with respect to that partition, i.e.,

$$\kappa(x) = \sum_{i=1}^r \kappa_i \chi_{P_i}(x).$$

Then equation (6) becomes

$$S\kappa = \mathbf{V}, \quad (7)$$

where $\kappa \in \mathbb{R}^r$ is a column vector containing the entries κ_i , $i = 1, \dots, r$, and $\mathbf{V} \in \mathbb{R}^{m^2}$ is obtained by writing the matrix $V \in \mathbb{R}^{m \times m}$ as a long column vector, i.e.,

$$\mathbf{V}_{(j-1)m+k} = V_{jk}, \quad j, k = 1, \dots, m.$$

$S \in \mathbb{R}^{m^2 \times r}$ is the so-called sensitivity matrix, its entries are given by

$$S_{(j-1)m+k,i} := - \int_{P_i} \nabla u_{\sigma_0}^{(j)} \cdot \nabla u_{\sigma_0}^{(k)} \, dx, \quad j, k = 1, \dots, m.$$

In this simple, yet well-established approach, the matrix structure of the measurements is completely ignored. As a consequence, erroneous voltage measurements on current-driven electrodes can simply be deleted from the linear system (7) by removing both, the corresponding lines in the sensitivity matrix, and the problematic entries in the right hand side of (7). Thus, one replaces (7) by the reduced system

$$\mathbb{S}\kappa = \mathbb{V}, \quad (8)$$

where $\mathbb{V} \in \mathbb{R}^{m(m-3)}$ denotes the difference data vector without the voltage measurements on current-driven electrodes, and $\mathbb{S} \in \mathbb{R}^{m(m-3) \times r}$ denotes the reduced sensitivity matrix, in which the lines corresponding to the problematic measurements are removed.

2.3. Matrix-based methods in EIT

Several new rigorously justified reconstruction approaches in EIT are based on utilizing the matrix structure of EIT measurements, cf. the overview in the introduction. In this subsection we summarize a recent linearized monotonicity-based method [32], that we will also use to numerically test our interpolation methods developed in the next section.

For the monotonicity method (but not for the interpolation method developed in the next section), we will restrict ourself to the so-called definite case that the conductivity change is either everywhere positive or everywhere negative. Without this assumption a more complicated variant of the method would be required, cf. [32].

Let S_i be the i -th column of the sensitivity matrix written as a $m \times m$ -matrix, i.e.,

$$S_i := - \begin{pmatrix} \int_{P_i} \nabla u_{\sigma_0}^{(1)} \cdot \nabla u_{\sigma_0}^{(1)} dx & \dots & \int_{P_i} \nabla u_{\sigma_0}^{(1)} \cdot \nabla u_{\sigma_0}^{(m)} dx \\ \vdots & & \vdots \\ \int_{P_i} \nabla u_{\sigma_0}^{(m)} \cdot \nabla u_{\sigma_0}^{(1)} dx & \dots & \int_{P_i} \nabla u_{\sigma_0}^{(m)} \cdot \nabla u_{\sigma_0}^{(m)} dx \end{pmatrix}. \quad (9)$$

When regarded as matrices and partially ordered with respect to matrix definiteness, the EIT measurements depend on the conductivity in a monotonous way. For all vectors $g = (g_k)_{k=1}^m \in \mathbb{R}^m$,

$$\begin{aligned} \int_{\Omega} \frac{\sigma_0}{\sigma} (\sigma_0 - \sigma) \left| \sum_{j=1}^m g_j \nabla u_{\sigma_0}^{(j)} \right|^2 dx &\geq g^T (U(\sigma) - U(\sigma_0)) g = g^T V g \\ &\geq \int_{\Omega} (\sigma_0 - \sigma) \left| \sum_{j=1}^m g_j \nabla u_{\sigma_0}^{(j)} \right|^2 dx. \end{aligned} \quad (10)$$

For the shunt model considered herein, the monotonicity relation (10) is proven in [28, lemma 3.1], see also [48, 40] for the origin of this inequality. Monotonicity relations similar to (10) have also been used to simplify the theoretical basis of the Factorization Method [27, 3], to prove theoretical uniqueness results, cf. [15, 25, 26, 34], and even to derive new hybrid tomography methods [28].

It follows from (10) that, for all $\beta \geq 0$,

$$\beta \chi_{P_i} \leq \sigma_0 - \sigma \quad \text{implies} \quad V \geq -\beta S_i, \quad \text{and} \quad (11)$$

$$\beta \chi_{P_i} \leq \frac{\sigma_0}{\sigma} (\sigma - \sigma_0) \quad \text{implies} \quad V \leq \beta S_i, \quad (12)$$

where the inequalities on the left hand sides of (11)–(12) are to be understood point-wise almost everywhere, and the inequalities on the right hand sides have to be interpreted in terms of matrix definiteness, i.e. $V \geq -\beta S_i$ means that the matrix $V + \beta S_i \in \mathbb{R}^{m \times m}$ possesses only non-negative eigenvalues.

The monotonicity inequality (10) also yields that

$$|V| = V \geq 0 \text{ for } \sigma \leq \sigma_0, \quad \text{and} \quad -|V| = V \leq 0 \text{ for } \sigma_0 \leq \sigma,$$

where $|V|$ denotes the matrix absolute value. For each pixel P_i , we define

$$\beta_i := \max\{\beta \geq 0 : \beta S_i \geq -|V|\}. \quad (13)$$

If the conductivity σ is either everywhere lower than the reference conductivity σ_0 (i.e., $\sigma \leq \sigma_0$), or everywhere larger (i.e., $\sigma \geq \sigma_0$), then (11)–(12) yield that for each pixel,

$$\inf_{x \in P_i} |\sigma(x) - \sigma_0(x)| > 0 \quad \text{implies} \quad \beta_i > 0.$$

Hence, the support of the function

$$x \mapsto \sum_{i=1}^r \beta_i \chi_{P_i}(x) \tag{14}$$

will contain the support of the conductivity change $|\sigma - \sigma_0|$ up to the pixel partition.

Moreover, one can show that, in the limit of infinitely many electrodes, when the measurements are given by the Neumann-Dirichlet-operators, $\beta_i = 0$ for each pixel that lies outside the outer support of $|\sigma_0 - \sigma|$, see [32]. Hence, in the limit of noiseless data on infinitely many electrodes, a plot of (14) will show where the conductivity σ differs from its reference state σ_0 . Let us stress that (even though linearized monotonicity tests are used), the non-linear shape reconstruction problem is being solved, cf. [32]. This is in accordance with the fact that shape information is in some sense unaffected by linearization errors, cf. [30].

Monotonicity-based methods require the full matrix of measurements. The definiteness tests in (13) do not seem possible without knowledge of the main diagonals of the measurement matrices, which contain the voltages on current-driven electrodes. In the next section we will develop a method that uses the geometry-specific smoothness of difference measurements in order to interpolate the missing voltages from the measurements on current-free electrodes.

3. Interpolation of missing electrode data in EIT

Though voltage measurements on current driven electrodes are usually considered erroneous, standard EIT systems such as the 32-channel Swisstom pioneer EIT system nevertheless allow the user to access these measurements. Hence, the simplest way to implement a method that relies on the measurements matrix structure is to simply ignore the problem and use the full measurement matrix as given by the EIT system. This approach has been taken for phantom experiment data in [76], and showed that the use of monotonicity-based constraints improves the reconstructions compared to a standard linearized approach (8). In the following, we will study how to interpolate the voltages on current-driven electrodes from the measurements on current-free electrodes.

3.1. Motivation for interpolating missing data

In many applications, small electrodes are used, the conductivity is assumed to be homogeneous in a neighbourhood of the boundary, and the conductivity change $\sigma - \sigma_0$ is assumed to occur with some distance to the boundary. In that case, the difference of the resulting potentials $v := u_\sigma - u_{\sigma_0}$ solves

$$\nabla \cdot (\sigma_0 \nabla v) = -\nabla \cdot (\sigma - \sigma_0) \nabla u_\sigma \quad \text{in } \Omega, \tag{15}$$

$$\int_{\mathcal{E}_l} \sigma \partial_\nu v \, ds = 0 \quad \text{for } l = 1, \dots, m, \quad (16)$$

$$\sigma \partial_\nu v = 0 \quad \text{on } \partial\Omega \setminus \bigcup_{l=1}^m \mathcal{E}_l, \quad (17)$$

$$v|_{\mathcal{E}_l} = \text{const.} \quad \forall l = 1, \dots, m, \quad (18)$$

If σ_0 is constant in a neighborhood of the boundary, then, in the limit of point electrodes (cf. [22]), v solves

$$\Delta v = 0 \quad \text{in a neighborhood of } \partial\Omega$$

with homogeneous Neumann boundary data $\partial_\nu v|_{\partial\Omega} = 0$. Hence, by standard elliptic regularity results, we can expect the voltage difference to be a very smooth function on $\partial\Omega$. This justifies to interpolate the missing or erroneous values on current-driven electrodes by the neighboring values on current-free electrodes.

3.2. Linear interpolation

We will first describe a simple linear interpolation approach that we will use as a benchmark for the more sophisticated approach described below. In a situation where the j -th electrode is positioned between and spatially close to the $(j-1)$ -th and the $(j+1)$ -th electrode, we may expect that the voltage difference $V_{j,j}$ should be close to the arithmetic mean of the values for the two neighboring electrode pairs, $V_{j,j-1}$ and $V_{j,j+1}$. Together with the fact that the measurement matrix should be symmetric and columns should sum up to zero, we thus obtain the following linear interpolation strategy.

Definition 3.1. *Given a symmetric EIT difference measurement matrix $V \in \mathbb{R}^{m \times m}$ (with possibly erroneous entries V_{jk} for $|j-k| \leq 1$), we define the linearly interpolated measurement matrix $V^{\text{lin}} \in \mathbb{R}^{m \times m}$ by solving the following equation system*

$$\begin{aligned} V_{jk}^{\text{lin}} &= V_{jk} && \text{for } |j-k| \geq 1 \text{ (modulo } m), \\ \sum_{j=1}^m V_{jk}^{\text{lin}} &= 0 && \text{for } k = 1, \dots, m, \\ V_{j,j-1}^{\text{lin}} &= V_{j-1,j}^{\text{lin}} && \text{for } j = 1, \dots, m, \\ V_{j,j}^{\text{lin}} &= \frac{1}{2}(V_{j-1,j}^{\text{lin}} + V_{j,j+1}^{\text{lin}}) && \text{for } j = 1, \dots, m. \end{aligned}$$

The linear equations are uniquely solvable for odd $m \in \mathbb{N}$. In the case of even $m \in \mathbb{N}$, the equations can be solved using the pseudo inverse.

3.3. Interpolation using geometry-specific smoothness

Our numerical examples in the next section show that the linearly interpolated measurements converge against the true measurements. However, this convergence is rather slow. Also, if the electrodes are not positioned in a single circle around an

imaging subject, the above linear interpolation method seems questionable and a more geometry-specific method should be used.

Our new interpolation approach is based on a more careful study of the arguments in subsection 3.1. The voltage difference $v = u_\sigma - u_{\sigma_0}$ solves the elliptic equation (15) with a source term on the support of the conductivity change $\sigma - \sigma_0$. The smoothness of $v|_{\partial\Omega}$ (and hence of the voltage measurements) will depend on how far the support of $\sigma - \sigma_0$ is located away from the boundary $\partial\Omega$. We will make use of this geometry-specific smoothness by assuming that we know an upper bound of the support, and demand that the interpolated measurements are consistent with a source term on this upper bound.

To make this idea precise, assume that we know a closed set B (with non-empty interior) so that

$$\text{supp}(\sigma - \sigma_0) \subseteq B \subseteq \Omega.$$

The j -th column in the matrix $V \in \mathbb{R}^{m \times m}$ contains the difference measurements

$$V_{jk} = v^{(k)}|_{\mathcal{E}_j} - v^{(k)}|_{\mathcal{E}_{j+1}},$$

where $v^{(k)}$ solves

$$\nabla \cdot (\sigma_0 \nabla v^{(k)}) = \nabla \cdot F^{(k)}, \quad (19)$$

with $F^{(k)} := -(\sigma - \sigma_0) \nabla u_\sigma^{(k)} \in L^2(B)^n$, and the boundary conditions (16)–(18).

Our new interpolation technique aims to fill in the missing data in such a way that (19) is fulfilled with the smallest possible source term $F^{(j)} \in L^2(B)$. Together with the symmetry and zero column sum condition, we thus obtain the following geometry-specific interpolation strategy.

Definition 3.2. *Let $V \in \mathbb{R}^{m \times m}$ be a symmetric EIT difference measurement matrix (with possibly erroneous entries V_{jk} for $|j-k| \leq 1$). We say that $F^{(1)}, \dots, F^{(m)} \in L^2(B)^n$ are minimal measurement-consistent source terms if they minimize*

$$\sum_{j=1}^m \|F^{(j)}\|_{L^2(B)^n}^2 \rightarrow \min!$$

under the constraint that the measurements constructed from these sources fulfill the interpolation, symmetry and zero column sum condition, i.e. with respective solutions $v^{(k)}$ of $\nabla \cdot (\sigma_0 \nabla v^{(k)}) = \nabla \cdot F^{(k)}$, (16)–(18),

$$V_{jk}^{\text{geom}} := v^{(k)}|_{\mathcal{E}_j} - v^{(k)}|_{\mathcal{E}_{j+1}},$$

must fulfill

$$V_{jk}^{\text{geom}} = V_{jk} \quad \text{for } |j-k| \geq 1 \text{ (modulo } m), \quad (20)$$

$$\sum_{j=1}^m V_{jk}^{\text{geom}} = 0 \quad \text{for } k = 1, \dots, m, \quad (21)$$

$$V_{j,j-1}^{\text{geom}} = V_{j-1,j}^{\text{geom}} \quad \text{for } j = 1, \dots, m. \quad (22)$$

The matrix V^{geom} constructed from measurement-consistent source terms is called the geometrically interpolated measurement matrix.

Remark 3.3. Definition 3.2 can be interpreted as a minimum norm interpolation in problem-specific abstract smoothness classes. Let us introduce

$$\tilde{K}_B : L^2(B)^n \rightarrow L^2(\partial\Omega), \quad F \mapsto f := v|_{\partial\Omega},$$

where $v \in H^1(\Omega)$ solves the source problem

$$\nabla \cdot (\sigma_0 \nabla v) = \nabla \cdot F, \tag{23}$$

with boundary conditions (16)–(18). Applying \tilde{K}_B entrywise to a m -tuple of functions in $L^2(B)^n$ we obtain the operator

$$K_B : (L^2(B)^n)^m \rightarrow L^2(\partial\Omega)^m, \quad (F^{(k)})_{k=1}^m \mapsto \left(\tilde{K}_B(F^{(k)}) \right)_{k=1}^m,$$

and define the space

$$H_B := \mathcal{R}(K_B) \subseteq L^2(\partial\Omega)^m.$$

with the range space norm

$$\| (f^{(k)})_{k=1}^m \|_{H_B} := \inf \{ \| (F^{(k)})_{k=1}^m \|_{(L^2(B)^n)^m} : f^{(k)} = \tilde{K}_B(F^{(k)}) \forall k \}.$$

For two open sets B_1, B_2 , with $\bar{B}_1 \subseteq B_2$, a standard mollification argument shows that every solution of (23) with source term $F \in L^2(B_1)^n$ also solves (23) with a source term in $H^1(B_2)^n$. Since $H^1(B_2)^n$ is compactly embedded in $L^2(B_2)^n$, it follows that the range space H_{B_1} is compactly embedded in H_{B_2} . Hence, analogously to the use of source conditions in regularization theory, the spaces H_B can be interpreted as abstract smoothness classes which formalize the intuitive fact that smaller sources generate smoother boundary potentials.

In that formalism, the geometrically interpolated measurement matrix in definition 3.2 is obtained from evaluating the minimum norm interpolant in H_B under the additional constraint of a symmetry and zero column sum condition.

We will now show that the geometrically interpolated matrix is unique and that it can be obtained in an easy and computationally cheap way. To that end, we assume that σ_0 fulfills a unique continuation property (UCP), which means that every solution of $\nabla \cdot (\sigma_0 \nabla u_0) = 0$ that is constant on an open subset of Ω must be constant on all of Ω . Also, we assume that B is chosen consistent with the pixel partition, i.e.,

$$B = \bigcup_{P_i \subseteq B} P_i.$$

As in subsection 2.3, $S_i \in \mathbb{R}^{m \times m}$ denotes the sensitivity matrix for the i -th pixel, i.e. the i -th column of the sensitivity matrix written as a $m \times m$ -matrix, cf. (9). Summing up all elements in B we define

$$S_B = \sum_{i: P_i \subseteq B} S_i \in \mathbb{R}^{m \times m}.$$

$S_B^+ \in \mathbb{R}^{m \times m}$ denotes the (Moore-Penrose-)pseudoinverse of S_B . $e_j \in \mathbb{R}^m$ is the j -th unit vector.

Theorem 3.4. *There exists a unique geometrically interpolated measurement matrix $V^{\text{geom}} \in \mathbb{R}^{m \times m}$. It is the unique minimizer of*

$$-\sum_{j=1}^m e_j^T (V^{\text{geom}})^T S_B^+ V^{\text{geom}} e_j \rightarrow \min!$$

under the constraints (20)–(22).

Theorem 3.4 is proven in the next subsection.

Remark 3.5. *The minimization problem in theorem 3.4 can be solved analytically. Let $V \in \mathbb{R}^{m \times m}$ be a symmetric EIT difference measurement matrix (with possibly erroneous entries V_{jk} for $|j - k| \leq 1$).*

$V^{\text{geom}} \in \mathbb{R}^{m \times m}$ fulfills the constraints (20)–(22) if and only if $V_{jk}^{\text{geom}} = V_{jk}$ for $|j - k| > 1$, and there exists a vector $w \in \mathbb{R}^m$ with

$$V_{j-1,j}^{\text{geom}} = w_j, \quad V_{j+1,j}^{\text{geom}} = w_{j+1}, \quad V_{j,j}^{\text{geom}} = -\sum_{l: |l-j|>1} V_{jl} - w_j - w_{j+1}. \quad (24)$$

Hence, we can write

$$V^{\text{geom}} e_j = A^{(j)} w + b^{(j)}$$

where $A^{(j)} \in \mathbb{R}^{m \times m}$ and $b^{(j)} \in \mathbb{R}^m$ are given by

$$A_{kl}^{(j)} = \delta_{k,j-1} \delta_{l,j} + \delta_{k,j+1} \delta_{l,j+1} - \delta_{k,j} \delta_{l,j} - \delta_{k,j} \delta_{l,j+1}$$

$$b_k^{(j)} = \begin{cases} V_{jk} & \text{for } |k - j| > 1, \\ 0 & \text{for } |k - j| = 1, \\ -\sum_{l: |l-j|>1} V_{jl} & \text{for } k = j. \end{cases}$$

Thus, with $A := -\sum_{j=1}^m (A^{(j)})^T S_B^+ A^{(j)}$ and $b := -\sum_{j=1}^m (A^{(j)})^T S_B^+ b^{(j)}$, the minimization problem is equivalent to minimizing

$$\frac{1}{2} w^T A w + b^T w \rightarrow \min!$$

for which the unique solution is given by $w = -A^{-1}b$. The values of V^{geom} are then determined by (20) and (24).

Remark 3.6. *Given r pixels and m electrodes, the computational effort to compute S_B is at most rm^2 , and all other computations in remark 3.5 are of the order $O(m^3)$. In a setting where the upper bound B and the sensitivity matrix S stay constant over several time-steps, a factorization of the matrix A can be precomputed. Thus the interpolation can be carried out in $O(m^2)$ steps, which is neglectable to the computational cost of reconstructing the conductivity. Hence, our new interpolation method is well suited for real-time imaging.*

Remark 3.7. *Note that our interpolation method uses the sensitivity matrix which also appears in linearized reconstruction methods. However, the interpolation method does not rely on a linearized approximation and interpolates the values of the true voltage difference (that depends non-linearly on the conductivity change).*

3.4. Proof of theorem 3.4

The rest of this section is devoted to proving theorem 3.4. We first introduce the so-called virtual measurement operator (cf., e.g., [27, 32])

$$L : L^2(B)^n \rightarrow \mathbb{R}^m, \quad F \mapsto (v|_{\mathcal{E}_k} - v|_{\mathcal{E}_{k+1}})_{k=1}^m \in \mathbb{R}^m,$$

where $v|_{\mathcal{E}_k} - v|_{\mathcal{E}_{k+1}}$, $k = 1, \dots, m$, is the measurement on the k -th electrode pair of the solution of the source problem

$$\nabla \cdot (\sigma_0 \nabla v) = \nabla \cdot F,$$

with boundary conditions (16)–(18). The next lemma summarizes some properties of L and its connection to the sensitivity matrix.

Lemma 3.8. (a) *The adjoint of L is given by*

$$L^* : \mathbb{R}^m \rightarrow L^2(B)^n, \quad L^* w = \sum_{j=1}^m w_j \nabla u_{\sigma_0}^{(j)}|_B \quad \text{for } w = (w_j)_{j=1}^m \in \mathbb{R}^m,$$

where $u_{\sigma_0}^{(j)}$ solves (1)–(4) with reference conductivity σ_0 and electric current driven through the j -th and $(j+1)$ -th electrode.

(b) *If B is consistent with the pixel partition, i.e., $B = \bigcup_{i: P_i \subseteq B} P_i$, then $S_B = -LL^*$.*

(c) *If σ_0 fulfills a UCP, then $\mathcal{R}(L) = \{v : \sum_{j=1}^m v_j = 0\} \subset \mathbb{R}^m$.*

Proof. (a) For the j -th unit vector $e_j \in \mathbb{R}^m$ and $F \in L^2(B)^n$ we have that

$$\begin{aligned} \int_B F \cdot (L^* e_j) \, dx &= (LF) \cdot e_j = v|_{\mathcal{E}_j} - v|_{\mathcal{E}_{j+1}} = \int_{\partial\Omega} \sigma_0 \partial_\nu u_{\sigma_0}^{(j)}|_{\partial\Omega} v|_{\partial\Omega} \, ds \\ &= \int_B F \cdot \nabla u_{\sigma_0}^{(j)} \, dx. \end{aligned}$$

(b) For the j -th and k -th unit vector $e_j, e_k \in \mathbb{R}^m$, we have that

$$\begin{aligned} \int_B (L^* e_j) \cdot (L^* e_k) \, dx &= \int_B \nabla u_{\sigma_0}^{(j)} \cdot \nabla u_{\sigma_0}^{(k)} \, dx \\ &= \sum_{i: P_i \subseteq B} \int_{P_i} \nabla u_{\sigma_0}^{(j)} \cdot \nabla u_{\sigma_0}^{(k)} \, dx = - \sum_{i: P_i \subseteq B} e_j^T S_i e_k^T = -e_j^T S_B e_k. \end{aligned}$$

(c) If σ_0 fulfills a UCP, then

$$0 = L^* w = \sum_{j=1}^m w_j \nabla u_{\sigma_0}^{(j)}|_B$$

is equivalent to $\sum_{j=1}^m w_j u_{\sigma_0}^{(j)} = \text{const.}$ on all of Ω .

Due to the definition of $u_{\sigma_0}^{(j)}$, we have that for each $l = 1, \dots, m$,

$$\begin{aligned} \int_{\mathcal{E}_l} \sigma_0 \partial_\nu \sum_{j=1}^m w_j u_{\sigma_0}^{(j)} \, ds &= \sum_{j=1}^m w_j \int_{\mathcal{E}_l} \sigma_0 \partial_\nu u_{\sigma_0}^{(j)} \, ds = \sum_{j=1}^m w_j (\delta_{j,l} - \delta_{j+1,l}) \\ &= w_l - w_{l+1} \end{aligned}$$

Hence, $\sum_{j=1}^m w_j u_{\sigma_0}^{(j)} = \text{const.}$ is equivalent to $w_1 = \dots = w_m = \text{const.}$, so that the assertion follows from $\mathcal{N}(L^*)^\perp = \mathcal{R}(L)$. □

Proof of theorem 3.4. Let $V \in \mathbb{R}^{n \times n}$ be symmetric difference EIT measurements (with possibly erroneous entries V_{jk} for $|j - k| \leq 1$). Due to lemma 3.8(c), the minimization problem in definition 3.2 is equivalent to finding $V^{\text{geom}} \in \mathbb{R}^{m \times m}$ that minimizes

$$\sum_{j=1}^m \|L^+ V^{\text{geom}} e_j\|_{L^2(B)^n}^2 \rightarrow \min!$$

under the constraints (20)–(22).

From lemma 3.8(b) it follows that $(L^+)^* L^+ = (LL^*)^+ = -S_B^+$, so that

$$\|L^+ V^{\text{geom}} e_j\|_{L^2(B)^n}^2 = -e_j^T (V^{\text{geom}})^T S_B^+ V^{\text{geom}} e_j.$$

Finally, for all $v \in \mathcal{R}(L)$ we have that

$$-v^T S_B^+ v = \|L^+ v\|_{L^2(B)^n}^2 \geq \frac{1}{\|L\|^2} \|LL^+ v\|_2^2 = \frac{1}{\|L\|^2} \|v\|_2^2,$$

so that

$$-\sum_{j=1}^m e_j^T (V^{\text{geom}})^T S_B^+ V^{\text{geom}} e_j \geq \frac{1}{\|L\|^2} \sum_{j=1}^m \|V^{\text{geom}} e_j\|_2^2 = \frac{1}{\|L\|^2} \|V^{\text{geom}}\|_{\text{Fro}}^2.$$

This shows that $-\sum_{j=1}^m e_j^T (V^{\text{geom}})^T S_B^+ V^{\text{geom}} e_j$ is a strictly coercive quadratic functional on the affine linear space of matrices fulfilling the constraints (20)–(22), which is a non-empty subset of $\mathcal{R}(L)$. Hence, the minimization problem is uniquely solvable. \square

4. Numerical results

In this section, we use the open source framework EIDORS developed by Adler and Lionheart [2], available on eidors.org, to numerically evaluate how good the interpolated measurements agree with the true ones and to test the performance of the matrix-based monotonicity method on interpolated data.

In our first example, the imaging domain Ω is the two-dimensional unit circle, the reference conductivity is $\sigma_0 = 1$, and the true conductivity is $\sigma = 1 + \chi_{D_1} + \chi_{D_2} + \chi_{D_3}$ with a larger half-ellipsoidal inclusion D_1 and two smaller circular inclusions D_2 and D_3 , see figure 1. We use EIDORS to simulate difference EIT measurements $V := U(\sigma) - U(\sigma_0) \in \mathbb{R}^{m \times m}$ for an adjacent-adjacent driving pattern with m electrodes (including voltages on current-driven electrodes) as described in section 2.1. The sensitivity matrix is also obtained from EIDORS but with another FEM grid to avoid an inverse crime. Figure 1 shows σ_0 and σ for a setting with $m = 32$ electrodes, and the FEM grids used for calculating the measurements $U(\sigma_0)$, $U(\sigma)$ and the sensitivity matrix S . The FEM grid for the latter is also used as the pixel partition for the reconstruction. Note that the choice of the reconstruction grid is ad-hoc in our examples in this section. For a fixed reconstruction grid, the monotonicity method will show the support of the conductivity difference up to the grid resolution in the limit of noiseless data and infinitely many electrodes. But it not yet clear how to choose an optimal reconstruction grid for a given

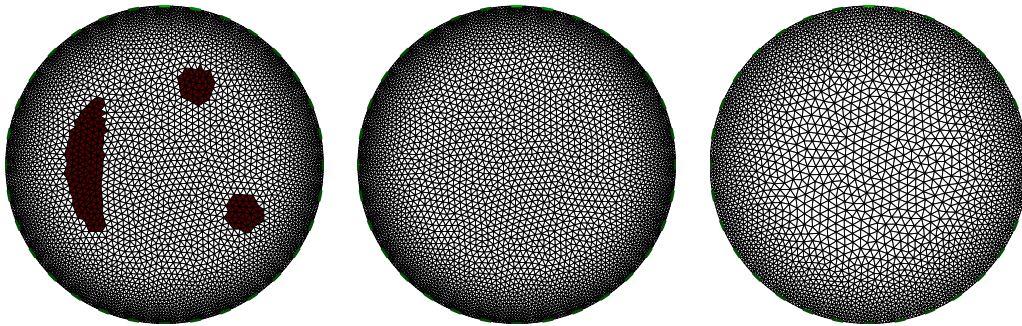


Figure 1. True conductivity σ (left image) and reference conductivity σ_0 (middle image) and the FEM grid used to calculate $U(\sigma)$ and $U(\sigma_0)$. The right image shows the FEM grid used to calculate the sensitivity matrix S .

amount of noise and number of electrodes (see however [33] for a method to evaluate whether certain reconstruction guarantees hold true on a given grid).

From the simulated EIT measurements $V \in \mathbb{R}^{m \times m}$, the entries corresponding to voltages on current-driven electrodes, V_{jk} with $|j - k| < 1$ (modulo m), are removed, and replaced using the simple linear interpolation method in subsection 3.2, and by our new geometrical interpolation method in subsection 3.3. For the latter, we use as upper bound B the union of all pixels which intersect an open ball (centered at the origin) with radius $r > 0$.

For a first impression of the performance of our new interpolation method consider figure 2. The black circles show the first 50 voltages taken columnwise from the difference EIT measurements V for $m = 24$ electrodes. The 24th entry corresponds to the voltage between the 24th and the 1st electrode with current applied between the 1st and 2nd electrode, the 25th-27th entry are the voltages between the 1st and the 2nd, the 2nd and the 3rd, and the 3rd and the 4th electrode, resp., while the current is driven between the 2nd and the 3rd electrode. Accordingly, these four entries are voltages on current driven electrodes. The red dashed line shows the values obtained by linear interpolation and the black solid line shows the values obtained by our new geometric interpolation method with $r = 0.7$. Our new method recovers the voltage on active electrodes much more precisely than the linear interpolation method.

Table 1 lists the relative interpolation errors in the Frobenius norm

$$\frac{\|V - V^{\text{lin}}\|_F}{\|V\|_F}, \quad \text{resp.}, \quad \frac{\|V - V^{\text{geom}}\|_F}{\|V\|_F}$$

for different electrode numbers m and radii r of the upper bound B . The results for our new interpolation using geometry-specific smoothness are clearly superior to linear interpolation. The interpolation error falls below 1% already for 32 electrodes and an upper bound B with $r = 0.8$.

We now study the feasibility of using interpolated measurements for the matrix-based monotonicity method described in subsection 2.3. We simulate the measurement

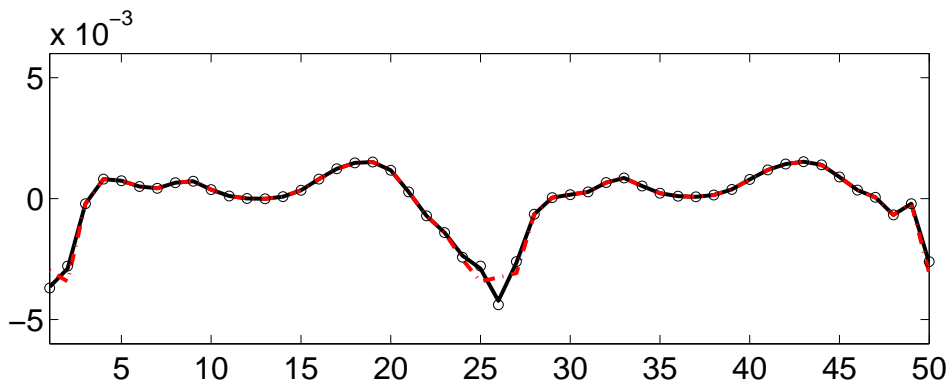


Figure 2. First 50 voltages measured in a setting with $m = 24$ electrodes including voltages on current driven electrodes (black circles) and the interpolated values using simple linear interpolation (red dashed line) and the new geometric interpolation method with $r = 0.7$ (black line).

	$m = 8$	$m = 16$	$m = 24$	$m = 32$	$m = 40$
linear interpolation	75.44%	32.29%	15.65%	8.23%	5.22%
geom. interpol. ($r = 0.9$)	79.07%	31.03%	11.00%	3.77%	1.48%
geom. interpol. ($r = 0.8$)	69.33%	18.09%	3.98%	0.67%	0.21%
geom. interpol. ($r = 0.7$)	61.88%	12.17%	2.48%	0.41%	0.16%

Table 1. Relative error (measured in the Frobenius norm) caused by replacing voltages on current driven electrodes by interpolated values.

matrix $V \in \mathbb{R}^{m \times m}$ for $m = 32$ electrodes (including the voltages on current-driven electrodes). Using a matrix $E \in \mathbb{R}^{m \times m}$ containing independently uniformly distributed random values in the interval $[-1, 1]$, we simulate noisy measurements by setting

$$V_\delta := V + \delta \|V\|_F \frac{E}{\|E\|_F}$$

for a given relative noise level $\delta > 0$. As above, we then remove the voltages on current-driven electrodes in V_δ and replace them by interpolated values using linear interpolation and our new geometry-specific interpolating method (again with $r = 0.7$, $r = 0.8$, and $r = 0.9$) to obtain the matrix V_δ^{lin} , resp., V_δ^{geom} . Our aim is to compare how much the monotonicity-based methods described in subsection 2.3 are affected by using the interpolated measurements V_δ^{lin} , resp., V_δ^{geom} instead of V_δ .

We implement the monotonicity method's indicator function (14) in the following form. As in (9), let $S_i \in \mathbb{R}^{m \times m}$ contain the entries of the i -th column of the sensitivity-matrix $S \in \mathbb{R}^{m^2 \times r}$. Since we deal with noisy measurements, we calculate the following regularized version of (13)

$$\beta_i^\delta := \max\{\beta \geq 0 : \beta S_i \geq -|V_\delta| - \delta \|V_\delta\|_F I\},$$

so that $\beta_i^\delta > 0$ is guaranteed to hold for every pixel inside the inclusions.

To calculate β_i^δ , note that $|V| + \delta \|V_\delta\|_F I$ is positive definite and thus possesses an invertible matrix square root $A \in \mathbb{R}^{m \times m}$ with $A^*A = |V_\delta| + \delta \|V_\delta\|_F I$. For each $\beta > 0$, we have that

$$\beta S_i + |V_\delta| + \delta \|V_\delta\|_F I = \beta S_i + A^*A = A^*(A^{-*}\beta S_i A^{-1} + I)A,$$

so that the definiteness condition $\beta S_i \geq -|V| - \delta \|V_\delta\|_F I$ is equivalent to

$$\beta A^{-*}S_i A^{-1} + I \geq 0. \quad (25)$$

Since obviously $S_i \leq 0$, the condition (25) is fulfilled if and only if no eigenvalue of $A^{-*}S_i A^{-1}$ is smaller (more negative) than $-\frac{1}{\beta}$. Hence,

$$\beta_i^\delta = -\frac{1}{\lambda_1}$$

where λ_1 is the smallest (most negative) eigenvalue of $A^{-*}S_i A^{-1} \in \mathbb{R}^{m \times m}$.

In the same way, we calculate the monotonicity indicator functions for the interpolated measurements V_δ^{lin} and V_δ^{geom} . Figure 3 shows (for $m = 32$ electrodes) the plot of $x \mapsto \sum_{j=1}^r \beta_j^\delta \chi_j(x)$ for measurements including the correct values on current-driven electrodes (first column), for geometrically interpolated measurements (with $r = 0.7$, $r = 0.8$ and $r = 0.9$ in the second, third and fourth column, respectively), and for linearly interpolated measurements (fifth column). The first line in figure 3 corresponds to the almost noiseless case ($\delta = 0.001\%$), for the second line we added relative noise with $\delta = 0.1\%$. The reconstructions are plotted with the EIDORS standard setting that all pixels with values less than 25% of the maximal value are set to transparent color. Additionally we cropped the color scale so that all pixels with values more than 50% of the maximal value are plotted with the same color. The results indicate that measurements on current-driven electrodes can well be replaced by interpolated measurements.

We also test our new interpolation method on a 3D example, where the imaging domain Ω is a cylinder to which electrodes are attached in 3 planes of k electrodes each. The reference conductivity is $\sigma_0 = 1$, and the true conductivity is $\sigma = 1 + \chi_{D_1} + \chi_{D_2}$ with a larger, vertically aligned, cylindrical inclusion D_1 and a smaller circular inclusion D_2 , see figure 4. We used EIDORS to simulate difference EIT measurements $V := U(\sigma) - U(\sigma_0) \in \mathbb{R}^{m \times m}$ for an adjacent-adjacent driving pattern with $m = 3k$ electrodes, including voltages on current-driven electrodes. Note that the driving patterns also contain measurements between electrodes on different planes. Figure 4 shows σ_0 and σ for a setting with $k = 24$ electrodes on each plane, and the FEM grids used for calculating the measurements $U(\sigma_0)$, $U(\sigma)$ and for calculating the sensitivity matrix S .

As in the two-dimensional case, we calculate the relative interpolation error that arises when measurements on current driven electrodes are removed and replaced using our new geometrical interpolation method. For the latter, we use as upper bound B the union of all pixels which intersect an open cylinder (centered at the origin) with radius $r = 0.7$, $r = 0.8$, and $r = 0.9$. Table 2 lists the relative interpolation errors in the Frobenius norm for a total number of $3 \cdot 16$, $3 \cdot 20$, $3 \cdot 24$, and $3 \cdot 28$ electrodes. The naive

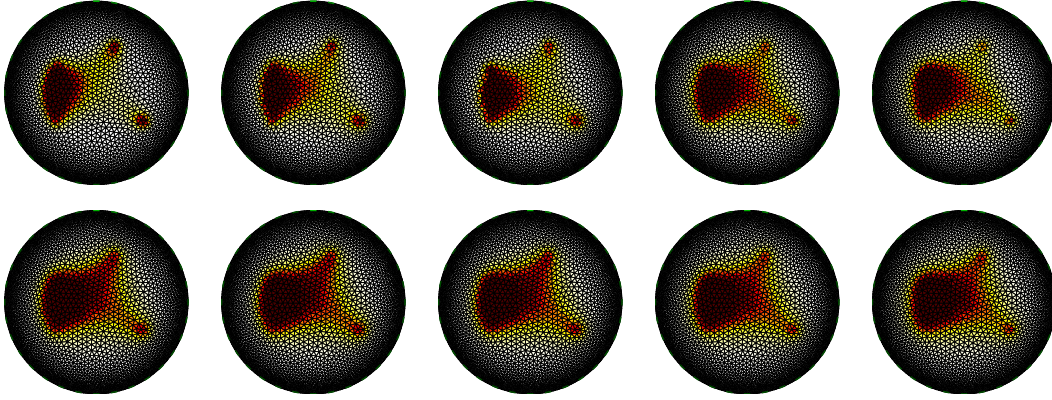


Figure 3. Monotonicity-based reconstructions using measurements on 32 electrodes including voltages on current driven electrodes (1st column) and after replacing them with geometrically interpolated values (with $r = 0.7$, $r = 0.8$ and $r = 0.9$ in the 2nd, 3rd and 4th column), and with linearly interpolated values (5th column). First line contains almost noiseless data ($\delta = 0.001\%$), second line contains relative noise with $\delta = 0.1\%$.

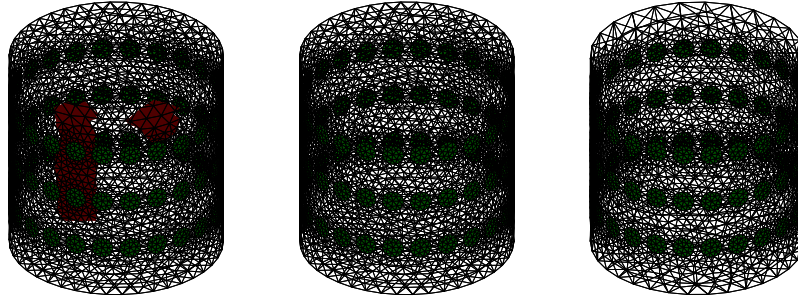


Figure 4. True conductivity σ (left image) and reference conductivity σ_0 (middle image) and the FEM grid used to calculate $U(\sigma)$ and $U(\sigma_0)$. The right image shows the FEM grid used to calculate the sensitivity matrix S .

	$m = 3 \cdot 16$	$m = 3 \cdot 20$	$m = 3 \cdot 24$	$m = 3 \cdot 28$
geom. interpol. ($r = 0.9$)	37.90%	23.93%	16.74%	7.88%
geom. interpol. ($r = 0.8$)	23.17%	11.82%	7.52%	3.17%
geom. interpol. ($r = 0.7$)	17.51%	8.04%	6.81%	2.56%

Table 2. Relative error (measured in the Frobenius norm) caused by replacing voltages on current driven electrodes by interpolated values.

application of our simple linear interpolation method fails on measurements between electrodes on different planes, and produced interpolation errors roughly around 40% for all our settings. Our new geometric interpolation method approximates the voltages on current driven electrodes well, the accuracy when using 3 planes of 28 electrodes is around 2.5%.

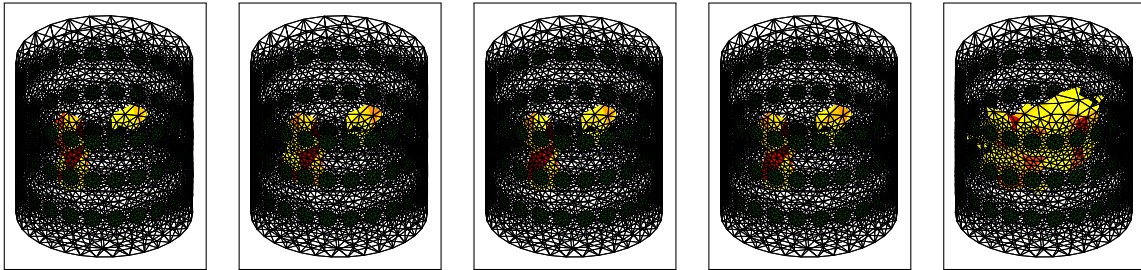


Figure 5. Monotonicity-based reconstructions using measurements on 32 electrodes including voltages on current driven electrodes (1st column) and after replacing them with geometrically interpolated values (with $r = 0.7$, $r = 0.8$ and $r = 0.9$ in the 2nd, 3rd and 4th column), and with linearly interpolated values (5th column).

Figure 5 shows the results of using the monotonicity method for the setting with $k = 24$ electrodes on each of 3 planes. We only calculated the indicator β_i for pixels between the upper and lower electrode plane. From left to right, the figure shows the reconstruction from measurements including active electrode data, and after replacing them with geometrically interpolated values using $r = 0.7$, $r = 0.8$ and $r = 0.9$, and after replacing them with linearly interpolated values. A relative noise of $\delta = 0.1\%$ was added to the measurements. The reconstructions are plotted with the EIDORS standard setting that all pixels with values less than 25% of the maximal value are set to transparent color. The monotonicity method works well with geometrically interpolated data. The reconstructions with interpolated data are almost indistinguishable from that using active electrode data, which is even better than what one would expect from the interpolation error in table 2. Moreover, even with naively linearly interpolated data, a very rough estimate of the convex hull of the inclusions is obtained.

5. Conclusion and discussion

Rigorously justified reconstruction methods for EIT, such as monotonicity-based methods, require voltage measurements on current-driven electrodes which are difficult to obtain in practice. In this work, we have developed a method to interpolate the voltages on current-driven electrodes from measurements on current-free electrodes for difference EIT settings. The interpolation is based on the geometry-specific smoothness of difference EIT data that arises from the fact that the difference potential solves an elliptic source problem.

Our method requires the a-priori knowledge of an upper bound of the support of the conductivity change. The implementation of our new interpolation method is particularly simple and computationally cheap. It suffices to identify the partition elements that belong to the upper bound of the support of the conductivity change, sum up the corresponding columns of the standard sensitivity matrix, and to invert matrices that are formed from this sum. The method is well suited for real-time imaging. In a setting with m electrodes and r partition elements, the computational cost is merely of

the order $O(m^2) + O(m^3)$ which lowers to $O(m^2)$ if geometry-specific quantities can be precomputed. Our numerical experiments show that the method achieves a very high interpolation accuracy, and that a monotonicity-based reconstruction method performs well with interpolated data.

We have formulated the method for the interpolation of voltages on current-driven electrodes in a real conductivity setting with adjacent-adjacent current driven patterns. The method seems also applicable to interpolate other missing or erroneous data (e.g., bad electrode data in practical measurements), and it should be extendable to complex conductivity (weighted frequency-difference) settings.

Our interpolation method is only applicable in difference EIT imaging and when the conductivity change occurs away from the boundary (which is arguably the most relevant case for recent commercial EIT applications). Voltage measurements in static EIT settings and voltage differences generated by a conductivity change at the boundary cannot be expected to possess the necessary smoothness properties to predict missing measurements by interpolation. Also, of course, interpolation is only necessary for EIT systems (such as the recent commercial ones) that do not provide reliable voltage measurements on current-driven electrodes.

Finally, let us stress that voltages on current-driven electrodes are only required by rigorously justified reconstruction methods such as the monotonicity method described herein. In practical applications, it is more common to use generic reconstruction algorithms that are based on minimizing a regularized data-fit functional, where missing measurements can simply be deleted from the residuum term. There are no rigorous convergence results for such generic optimization-based approaches, but they practically perform very well, and, so far, the stronger theoretical basis of rigorously justified methods has not lead to superior reconstructions in practice. Medical imaging algorithms must meet the highest standards, both in their practical performance and their theoretical justification. Hence, it seems highly desirable to develop practically well-working algorithms for which at least certain properties can also be theoretically guaranteed.

References

- [1] A. Adler, R. Gaburro, and W. Lionheart. Electrical impedance tomography. In *Handbook of Mathematical Methods in Imaging*, pages 599–654. Springer, 2011.
- [2] A. Adler and W. R. Lionheart. Uses and abuses of EIDORS: an extensible software base for EIT. *Physiological measurement*, 27(5):S25, 2006.
- [3] L. Arnold and B. Harrach. Unique shape detection in transient eddy current problems. *Inverse Problems*, 29(9):095004, 2013.
- [4] M. Azzouz, M. Hanke, C. Oesterlein, and K. Schilcher. The factorization method for electrical impedance tomography data from a new planar device. *International journal of biomedical imaging*, 2007, 2007.
- [5] D. Barber and B. Brown. Applied potential tomography. *J. Phys. E: Sci. Instrum.*, 17(9):723–733, 1984.
- [6] A. Barth, B. Harrach, N. Hyvönen, and L. Mustonen. Detecting stochastic inclusions in

- electrical impedance tomography. *submitted for publication. Preprint available online at www.mathematik.uni-stuttgart.de/oip.*
- [7] R. Bayford. Bioimpedance tomography (electrical impedance tomography). *Annu. Rev. Biomed. Eng.*, 8:63–91, 2006.
 - [8] L. Borcea. Electrical impedance tomography. *Inverse problems*, 18(6):99–136, 2002.
 - [9] L. Borcea. Addendum to ‘Electrical impedance tomography’. *Inverse Problems*, 19(4):997–998, 2003.
 - [10] M. Brühl and M. Hanke. Numerical implementation of two noniterative methods for locating inclusions by impedance tomography. *Inverse Problems*, 16:1029–1042, 2000.
 - [11] N. Chaulet, S. Arridge, T. Betcke, and D. Holder. The factorization method for three dimensional electrical impedance tomography. *Inverse Problems*, 30(4):045005, 2014.
 - [12] M. Cheney, D. Isaacson, and J. Newell. Electrical impedance tomography. *SIAM review*, 41(1):85–101, 1999.
 - [13] M. K. Choi, B. Harrach, and J. K. Seo. Regularizing a linearized EIT reconstruction method using a sensitivity-based factorization method. *Inverse Problems in Science and Engineering*, 22(7):1029–1044, 2014.
 - [14] B. Gebauer. The factorization method for real elliptic problems. *Z. Anal. Anwendungen*, 25:81–102, 2006.
 - [15] B. Gebauer. Localized potentials in electrical impedance tomography. *Inverse Probl. Imaging*, 2(2):251–269, 2008.
 - [16] B. Gebauer and N. Hyvönen. Factorization method and irregular inclusions in electrical impedance tomography. *Inverse Problems*, 23:2159–2170, 2007.
 - [17] H. Haddar and G. Migliorati. Numerical analysis of the factorization method for EIT with a piecewise constant uncertain background. *Inverse Problems*, 29(6):065009, 2013.
 - [18] H. Hakula and N. Hyvönen. On computation of test dipoles for factorization method. *BIT Num. Math.*, 49(1):75–91, 2009.
 - [19] R. Halter, A. Hartov, and K. D. Paulsen. Design and implementation of a high frequency electrical impedance tomography system. *Physiological measurement*, 25(1):379, 2004.
 - [20] R. J. Halter, A. Hartov, and K. D. Paulsen. A broadband high-frequency electrical impedance tomography system for breast imaging. *Biomedical Engineering, IEEE Transactions on*, 55(2):650–659, 2008.
 - [21] M. Hanke and M. Brühl. Recent progress in electrical impedance tomography. *Inverse Problems*, 19(6):S65–S90, 2003.
 - [22] M. Hanke, B. Harrach, and N. Hyvönen. Justification of point electrode models in electrical impedance tomography. *Mathematical Models and Methods in Applied Sciences*, 21(06):1395–1413, 2011.
 - [23] M. Hanke and A. Kirsch. Sampling methods. In O. Scherzer, editor, *Handbook of Mathematical Models in Imaging*, pages 501–550. Springer, 2011.
 - [24] M. Hanke and B. Schappel. The factorization method for electrical impedance tomography in the half-space. *SIAM J. Appl. Math.*, 68(4):907–924, 2008.
 - [25] B. Harrach. On uniqueness in diffuse optical tomography. *Inverse Problems*, 25:055010 (14pp), 2009.
 - [26] B. Harrach. Simultaneous determination of the diffusion and absorption coefficient from boundary data. *Inverse Probl. Imaging*, 6(4):663–679, 2012.
 - [27] B. Harrach. Recent progress on the factorization method for electrical impedance tomography. *Computational and mathematical methods in medicine*, 2013, 2013.
 - [28] B. Harrach, E. Lee, and M. Ullrich. Combining frequency-difference and ultrasound modulated electrical impedance tomography. *Inverse Problems*, 31(9):095003, 2015.
 - [29] B. Harrach and J. K. Seo. Detecting inclusions in electrical impedance tomography without reference measurements. *SIAM Journal on Applied Mathematics*, 69(6):1662–1681, 2009.
 - [30] B. Harrach and J. K. Seo. Exact shape-reconstruction by one-step linearization in electrical

- impedance tomography. *SIAM Journal on Mathematical Analysis*, 42(4):1505–1518, 2010.
- [31] B. Harrach, J. K. Seo, and E. J. Woo. Factorization method and its physical justification in frequency-difference electrical impedance tomography. *IEEE Trans. Med. Imaging*, 29(11):1918–1926, 2010.
- [32] B. Harrach and M. Ullrich. Monotonicity-based shape reconstruction in electrical impedance tomography. *SIAM Journal on Mathematical Analysis*, 45(6):3382–3403, 2013.
- [33] B. Harrach and M. Ullrich. Resolution guarantees in electrical impedance tomography. *IEEE Trans. Med. Imaging*, 34:1513–1521, 2015.
- [34] B. Harrach and M. Ullrich. Local uniqueness for an inverse boundary value problem with partial data. *Proc. Amer. Math. Soc.*, to appear.
- [35] R. Henderson and J. Webster. An impedance camera for spatially specific measurements of the thorax. *IEEE Trans. Biomed. Eng.*, BME-25(3):250–254, 1978.
- [36] D. Holder. *Electrical Impedance Tomography: Methods, History and Applications*. IOP Publishing, Bristol, UK, 2005.
- [37] N. Hyvönen, H. Hakula, and S. Pursiainen. Numerical implementation of the factorization method within the complete electrode model of electrical impedance tomography. *Inverse Probl. Imaging*, 1(2):299–317, 2007.
- [38] T. Ide, H. Isozaki, S. Nakata, and S. Siltanen. Local detection of three-dimensional inclusions in electrical impedance tomography. *Inverse Problems*, 26(3):035001, 17, 2010.
- [39] T. Ide, H. Isozaki, S. Nakata, S. Siltanen, and G. Uhlmann. Probing for electrical inclusions with complex spherical waves. *Comm. Pure Appl. Math.*, 60:1415–1442, 2007.
- [40] M. Ikehata. Size estimation of inclusion. *J. Inverse Ill-Posed Probl.*, 6(2):127–140, 1998.
- [41] M. Ikehata. How to draw a picture of an unknown inclusion from boundary measurements. Two mathematical inversion algorithms. *J. Inverse Ill-Posed Probl.*, 7(3):255–271, 1999.
- [42] M. Ikehata. Reconstruction of the support function for inclusion from boundary measurements. *J. Inverse Ill-Posed Probl.*, 8(4):367–378, 2000.
- [43] M. Ikehata. A regularized extraction formula in the enclosure method. *Inverse Problems*, 18(2):435, 2002.
- [44] M. Ikehata and S. Siltanen. Numerical method for finding the convex hull of an inclusion in conductivity from boundary measurements. *Inverse Problems*, 16:1043, 2000.
- [45] M. Ikehata and S. Siltanen. Electrical impedance tomography and Mittag-Leffler’s function. *Inverse Problems*, 20:1325, 2004.
- [46] D. Isaacson, J. Mueller, J. Newell, and S. Siltanen. Reconstructions of chest phantoms by the D-bar method for electrical impedance tomography. *IEEE Trans. Med. Imaging*, 23(7):821–828, 2004.
- [47] D. Isaacson, J. Mueller, J. Newell, and S. Siltanen. Imaging cardiac activity by the D-bar method for electrical impedance tomography. *Physiol. Meas.*, 27(5):S43, 2006.
- [48] H. Kang, J. K. Seo, and D. Sheen. The inverse conductivity problem with one measurement: stability and estimation of size. *SIAM J. Math. Anal.*, 28(6):1389–1405, 1997.
- [49] A. Kirsch. The factorization method for a class of inverse elliptic problems. *Math. Nachr.*, 278(3):258–277, 2005.
- [50] A. Kirsch and N. Grinberg. *The factorization method for inverse problems*, volume 36 of *Oxford Lecture Ser. Math. Appl.* Oxford University Press, Oxford, 2008.
- [51] K. Knudsen. *On the inverse conductivity problem*. PhD thesis, Department of Mathematical Science, Aalborg University, 2002.
- [52] K. Knudsen. A new direct method for reconstructing isotropic conductivities in the plane. *Physiol. Meas.*, 24(2):391, 2003.
- [53] K. Knudsen, M. Lassas, J. Mueller, and S. Siltanen. D-bar method for electrical impedance tomography with discontinuous conductivities. *SIAM J. Appl. Math.*, 67(3):893–913, 2007.
- [54] K. Knudsen, M. Lassas, J. Mueller, and S. Siltanen. Regularized D-bar method for the inverse conductivity problem. *Inverse Probl. Imaging*, 35(4):599, 2009.

- [55] K. Knudsen, J. Mueller, and S. Siltanen. Numerical solution method for the dbar-equation in the plane. *J. Comput. Phys.*, 198(2):500–517, 2004.
- [56] K. Knudsen and A. Tamasan. Reconstruction of less regular conductivities in the plane. *Comm. Partial Differential Equations*, 29(3-4):361–381, 2005.
- [57] A. Lechleiter, N. Hyvönen, and H. Hakula. The factorization method applied to the complete electrode model of impedance tomography. *SIAM Journal on Applied Mathematics*, 68(4):1097–1121, 2008.
- [58] A. Lechleiter and A. Rieder. Newton regularizations for impedance tomography: convergence by local injectivity. *Inverse Problems*, 24(6):065009, 2008.
- [59] W. R. B. Lionheart. EIT reconstruction algorithms: pitfalls, challenges and recent developments. *Physiol. Meas.*, 25:125–142, 2004.
- [60] O. G. Martinsen and S. Grimnes. *Bioimpedance and bioelectricity basics*. Academic press, 2011.
- [61] P. Metherall, D. Barber, R. Smallwood, and B. Brown. Three dimensional electrical impedance tomography. *Nature*, 380(6574):509–512, 1996.
- [62] A. Nachman. Global uniqueness for a two-dimensional inverse boundary value problem. *Ann. of Math. (2)*, 143(1):71–96, 1996.
- [63] A. I. Nachman, L. Päivärinta, and A. Teirilä. On imaging obstacles inside inhomogeneous media. *J. Funct. Anal.*, 252(2):490–516, 2007.
- [64] J. Newell, D. G. Gisser, and D. Isaacson. An electric current tomograph. *IEEE Trans. Biomed. Eng.*, 35(10):828–833, 1988.
- [65] G. J. Saulnier, N. Liu, C. Tamma, H. Xia, T.-J. Kao, J. Newell, and D. Isaacson. An electrical impedance spectroscopy system for breast cancer detection. In *Engineering in Medicine and Biology Society, 2007. EMBS 2007. 29th Annual International Conference of the IEEE*, pages 4154–4157. IEEE, 2007.
- [66] S. Schmitt. The factorization method for EIT in the case of mixed inclusions. *Inverse Problems*, 25(6):065012, 20, 2009.
- [67] S. Schmitt and A. Kirsch. A factorization scheme for determining conductivity contrasts in impedance tomography. *Inverse Problems*, 27:095005, 2011.
- [68] J. K. Seo, J. Lee, H. Zribi, S. W. Kim, and E. J. Woo. Frequency-difference electrical impedance tomography (fdEIT): Algorithm development and feasibility study. *Physiol. Meas.*, 29:929–944, 2008.
- [69] J. K. Seo and E. J. Woo. Electrical impedance tomography. *Nonlinear Inverse Problems in Imaging*, pages 195–249, 2013.
- [70] S. Siltanen, J. Mueller, and D. Isaacson. An implementation of the reconstruction algorithm of A Nachman for the 2D inverse conductivity problem. *Inverse Problems*, 16(3):681, 2000.
- [71] A. Tamburrino. Monotonicity based imaging methods for elliptic and parabolic inverse problems. *J. Inverse Ill-Posed Probl.*, 14(6):633–642, 2006.
- [72] A. Tamburrino and G. Rubinacci. A new non-iterative inversion method for electrical resistance tomography. *Inverse Problems*, 18(6):1809–1829, 2002.
- [73] G. Uhlmann. Electrical impedance tomography and Calderón’s problem. *Inverse problems*, 25(12):123011, 2009.
- [74] G. Uhlmann and J.-N. Wang. Reconstructing discontinuities using complex geometrical optics solutions. *SIAM J. Appl. Math.*, 68(4):1026–1044, 2008.
- [75] A. Wexler, B. Fry, and M. Neuman. Impedance-computed tomography algorithm and system. *Applied optics*, 24(23):3985–3992, 1985.
- [76] L. Zhou, B. Harrach, and J. K. Seo. Monotonicity-based electrical impedance tomography lung imaging. *submitted for publication. Preprint available online at www.mathematik.uni-stuttgart.de/oip.*